

# Latent Heating and Mixing due to Entrainment in Tropical Deep Convection

CLAYTON J. MCGEE AND SUSAN C. VAN DEN HEEVER

*Department of Atmospheric Science, Colorado State University, Fort Collins, Colorado*

(Manuscript received 13 May 2013, in final form 31 July 2013)

## ABSTRACT

Recent studies have noted the role of latent heating above the freezing level in reconciling Riehl and Malkus' hot tower hypothesis (HTH) with evidence of diluted tropical deep convective cores. This study evaluates recent modifications to the HTH through Lagrangian trajectory analysis of deep convective cores in an idealized, high-resolution cloud-resolving model (CRM) simulation that uses a sophisticated two-moment microphysical scheme. A line of tropical convective cells develops within a finer nested grid whose boundary conditions are obtained from a large-domain CRM simulation approaching radiative convective equilibrium (RCE). Microphysical impacts on latent heating and equivalent potential temperature ( $\theta_e$ ) are analyzed along trajectories ascending within convective regions of the high-resolution nested grid. Changes in  $\theta_e$  along backward trajectories are partitioned into contributions from latent heating due to ice processes and a residual term that is shown to be an approximate representation of mixing. The simulations demonstrate that mixing with dry environmental air decreases  $\theta_e$  along ascending trajectories below the freezing level, while latent heating due to freezing and vapor deposition increase  $\theta_e$  above the freezing level. Latent heating contributions along trajectories from cloud nucleation, condensation, evaporation, freezing, deposition, and sublimation are also quantified. Finally, the source regions of trajectories reaching the upper troposphere are identified. Much of the air ascending within convective updrafts originates from above the lowest 2 km AGL, but the strongest updrafts are composed of air from closer to the surface. The importance of both boundary layer and midlevel inflow in moist environments is underscored in this study.

## 1. Introduction

Tropical deep convection is a driving force behind the Hadley circulation, which is characterized by an ascending branch near equatorial latitudes and a descending branch in the subtropics. Riehl and Malkus (1958) developed what later became known as the hot tower hypothesis (HTH), in which the Hadley circulation was hypothesized to be driven by a population of undiluted deep convective cores, or "hot towers." However, measurements of tropical deep convective updrafts made during field campaigns provided little evidence of undiluted convective cores (LeMone and Zipser 1980; Zipser and LeMone 1980; Igau et al. 1999; Anderson et al. 2005; and others). Based on observations of updraft intensities, Zipser (2003) demonstrated that parcels likely require additional buoyancy provided by latent heating

above the freezing level in order to reach the upper troposphere.

To provide further evidence for the claims in Zipser (2003), Fierro et al. (2009) performed a high-resolution modeling study of a tropical squall line and quantified changes in equivalent potential temperature ( $\theta_e$ ) as a function of height along trajectories ascending from the boundary layer. Fierro et al. (2009) noted that  $\theta_e$  decreases in the lowest few kilometers owing to the mixing of drier environmental air into the convection and increases for many parcels above the freezing level. As a result, they presented a modified definition of hot towers as "any deep convective tower rooted on the boundary layer and topping in the upper troposphere," regardless of the degree of dilution. Romps and Kuang (2010) also noted that the latent heat of fusion allows parcels that are diluted to reach the tropopause, and Yeo and Romps (2013) demonstrated that deep convective clouds are heavily diluted and that the origin height of the convective air is well above cloud base. Fierro et al. (2012) quantified the specific latent heating processes that could lead to the vertical distribution of

---

*Corresponding author address:* Clayton J. McGee, Department of Atmospheric Science, Colorado State University, 1371 Campus Delivery, Fort Collins, CO 80523.  
E-mail: cjmgee@atmos.colostate.edu

$\theta_e$  reported in Fierro et al. (2009). Their study demonstrated that latent heating along a representative trajectory showed significant amounts of freezing and vapor deposition onto ice species above the freezing level.

The microphysical scheme within a cloud-resolving model may have a large effect on simulated latent heating rates. Two-moment (2M) bulk microphysical schemes usually prognose hydrometeor mixing ratio and number concentration, while one-moment (1M) schemes typically prognose only the hydrometeor mixing ratio. The resulting differences in hydrometeor size distributions between 1M and 2M schemes mean that resulting latent heating and cooling rates are different as well, since changes in hydrometeor size distributions can strongly affect the rates of latent heating processes (van den Heever and Cotton 2004; Gilmore et al. 2004; Morrison et al. 2009). Morrison et al. (2009) noted that within a midlatitude squall line, the amount of evaporation (and hence precipitation) in the stratiform region was significantly influenced by differences in the drop size distributions produced by 1M and 2M schemes. In idealized supercell simulations, Dawson et al. (2010) noted that 2M schemes produced evaporatively generated cold-pool strengths more in line with observations than 1M schemes. Adams-Selin et al. (2013) also noted large differences in the dynamics and microphysics of bow echoes when comparing 1M and 2M schemes.

In a modeling study of tropical deep convection, Johnson et al. (2002) used the 1M scheme described in Tao and Simpson (1993). The Johnson et al. (2002) results showed that condensation/evaporation and vapor deposition/sublimation were the primary contributors to latent heating below and above the freezing level, respectively, and Tao et al. (1995) showed the reduced importance of melting in tropical squall lines compared to midlatitude squall lines. In Fierro et al. (2012), latent heating along the representative trajectory in Fierro et al. (2012) above the freezing level showed significant amounts of freezing and a nonnegligible but considerably lower heating rate from vapor deposition. This stands in contrast to the results of Johnson et al. (2002), despite the fact that both studies used 1M schemes. 1M schemes have been improving in their representation of latent heating and reflectivity in deep convection, as evidenced by Lang et al. (2007, 2011). The differences between Fierro et al. (2012) and Johnson et al. (2002) may arise from the deficiencies with the microphysical scheme employed in Fierro et al. (2012), as acknowledged in their study. For example, raindrops were frozen instantaneously and completely when they entered air temperatures below 0°C. This formulation presumably led to what they observed as a localized maximum in latent heating immediately above the freezing level.

Fierro et al. (2012) also noted that their simulation was overpredicting graupel mixing ratios just above the freezing level compared with microphysical observations made of tropical convection by Petersen et al. (1999). Also, the microphysical scheme used by Fierro et al. (2012) employed a monodisperse cloud droplet size spectrum. This prescription of cloud droplet size likely yielded a different vertical profile of latent heating compared with what would have been expected if an inverse exponential or gamma size distribution of cloud droplet sizes had been allowed. Through impacts on the diabatic processes of evaporation and condensation, all of these assumptions may have important impacts on the vertical profile of latent heating within deep convection, and, hence, ultimately on  $\theta_e$ .

The 2M bin-emulating microphysical scheme employed in this study within the Regional Atmospheric Modeling System (RAMS) (Pielke et al. 1992; Cotton et al. 2003) allows for the explicit prediction of both hydrometeor mixing ratio and number concentration. A bimodal cloud droplet spectrum is allowed, which is a more realistic size distribution than a monodisperse droplet population (Hobbs et al. 1980; Saleeby and Cotton 2004); this may have important implications for the rates of condensation, evaporation, riming of cloud water, and vapor deposition. Also, there is no assumption in the 2M RAMS scheme that the freezing of rainwater above the freezing level is instantaneous. Given the important role that microphysical schemes can have on the latent heating and  $\theta_e$  profiles within deep convection, it is advantageous to extend the Fierro et al. (2012) study by using the sophisticated 2M scheme within RAMS to further investigate the microphysical processes that contribute to latent heating in tropical deep convection.

The forward trajectories released in Fierro et al. (2009) were initialized within the boundary layer, but there may be reason to question the appropriateness of having the near surface as the only source region; the degree to which tropical deep convective clouds consist of air entrained from above the boundary layer is not entirely apparent. Efforts have been made to understand the source regions of deep convective air. Under the “crossover zone” model put forward by Betts (1976) and Zipser (1977), primarily only boundary layer parcels were available to ascend to the upper troposphere. However, in an analysis of Doppler radar measurements made of deep convection during the Tropical Ocean and Global Atmosphere Coupled Ocean–Atmosphere Response Experiment (TOGA COARE), Kingsmill and Houze (1999) showed that deep-layer inflows into updrafts were quite common. Observations and a modeling simulation by Bryan and Fritsch (2000) showed similar results. Mecham et al. (2002) investigated the importance

of deep inflow by comparing two simulated convective systems from TOGA COARE that differed in terms of midlevel moisture. Their simulations showed that the moister case had much deeper inflow than the drier case. Lucas and Zipser (2000) documented substantial variability in environmental moisture during TOGA COARE among active convective events. Thus, it is likely that the heights of convective inflow vary significantly across different environments. This study quantifies the relative importance of near-surface versus deeper-layer inflow by initiating parcel trajectories at all levels in front of a line of convective cells and tracking them through their lifetimes.

The cloud-resolving model (CRM) simulation in this study is performed at high resolution in an environment that approaches radiative–convective equilibrium (RCE), which is a typical state of the tropical atmosphere and has been used to simulate deep convection in many previous studies (Tompkins and Craig 1998; Xu and Randall 1999; Grabowski and Moncrieff 2004; Posselt et al. 2008, 2012; Stephens et al. 2008; van den Heever et al. 2011; Storer and van den Heever 2013). Several CRM studies in RCE have been performed using RAMS. Stephens et al. (2008) demonstrated the importance of cloud-radiative feedbacks due to high clouds created by convective outflow. Posselt et al. (2008) captured the trimodal distribution of tropical convection and the three stable layers reported by Johnson et al. (1999) and underscored the importance of large-scale subsidence in maintaining the tropical stable layer near the freezing level. Van den Heever et al. (2011) and Storer and van den Heever (2013) investigated the role of aerosol particles on tropical convection, and Posselt et al. (2012) showed how changes in sea surface temperature might affect convective frequency and intensity in a warming climate. Modeling tropical convection in the large domains approaching RCE in the studies above has several advantages. The domain is large enough to capture the large-scale interactions between moist and dry regions. These large-scale circulations are somewhat analogous to the Walker circulation and therefore may be a good way of simulating convection within the equatorial trough zone. Further specifics about the model setup are discussed in section 2, along with methodology for analyzing latent heating and mixing along parcel trajectories. Results are presented in section 3, and conclusions and implications are discussed in section 4.

## 2. Methodology

### a. Model setup

This study uses RAMS (Cotton et al. 2003; Saleeby and van den Heever 2013) to simulate oceanic tropical

TABLE 1. Characteristics of the RCE simulation outer grid.

Characteristic	Description
Initial sounding	0000 UTC 5 Dec 1992 TOGA COARE, horizontally homogeneous
Initiation mechanism	Randomized 0.1-K temperature perturbations near surface
Domain size	3000 km × 200 km × 24.8 km
Domain resolution	1-km horizontal grid spacing, stretched grid with 65 levels
Location and time	10°N, 40°E (160 min ahead of UTC)
Boundary conditions	Doubly periodic
Time step	5 s
Surface type	Fixed SST of 300 K
Coriolis force	Off
Radiation	Two-stream radiation scheme (Harrington et al. 1999)
Turbulence	Smagorinsky (1963) deformation $K$ closure
Microphysics	Two-moment bin-emulating scheme (Saleeby and Cotton 2004)
Aerosols	Uniformly set to 100 cm <sup>-3</sup>

deep convection within an idealized, large-domain, high-resolution framework that approaches RCE. The model domain initially consists of a single coarse grid, the specifications of which are described in Table 1. At 1-km grid spacing, the coarse grid is of cloud-resolving resolution but is too coarse to adequately represent a significant amount of organized turbulent convective overturning (Bryan et al. 2003). Therefore, as the simulation approaches RCE, a finer nested grid with horizontal grid spacing of 250 m is placed in the eastern third of the domain where a line of convective cells develops by the end of day 15, as shown in Fig. 1a. The finer grid is enlarged in Fig. 1b. In total, there are 802 × 482 grid points in the horizontal and 128 vertical levels on the finer nested grid. At the history restart, the time step is reduced to 3 s for both grids. The finer grid simulation is run for an additional 100 min, during which two-way communication occurs between the two grids. The 90 min (extending from 2310 UTC on day 15 to 0040 UTC on day 16) constitutes the time during which intensive analysis is performed.

### b. Environmental conditions

The convection that develops by the end of day 15 is oriented north to south and travels to the east at about 5 m s<sup>-1</sup> along a large-scale line of convergence. A cross section of meridionally averaged zonal wind and total condensate is shown in Fig. 2 at 2310 UTC, which is the start of the analysis period. Easterly inflow and westerly lower-level cold-pool-driven outflow are evident, along with upper-level divergent outflow. The inflow region of the storm is quite deep, extending to about 8 km AGL.

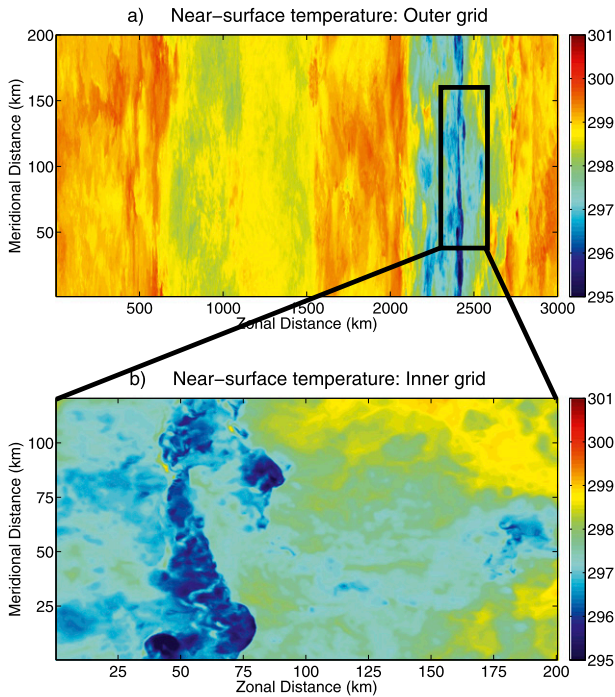


FIG. 1. Plan view of near-surface temperature for the (a) outer grid and (b) inner grid at 2310 UTC. The location of the nested grid in the larger domain is shown by the black square.

Convective cells that form along the convergence line are generally characterized by vertical velocities up to  $15 \text{ m s}^{-1}$  (although a few cells' vertical velocities reach near  $25 \text{ m s}^{-1}$  in the upper troposphere). Cloud base is approximately 400 m AGL, which is in the range of what is possible in tropical maritime environments. The

freezing level in the domain is approximately 4.6 km. The values for updraft speeds, cloud base height, and freezing level height appear to be highly comparable to typical values in the tropics. This lends credence to the idealized convection in this study serving to first order as an acceptable representation of some observed tropical deep convective systems.

*c. Forward trajectory initialization*

This study relies on Lagrangian trajectory analysis of both forward and backward trajectories. The forward trajectories are initiated in a “curtain” between 10 and 50 km from the southern boundary and 5 km ahead of the location of the surface cold pool at 2310 UTC (Fig. 3). The surface cold-pool gust front is calculated as the location where wind direction at the first model level above the surface switches from westerly to easterly. Trajectories are placed 1 km apart in the meridional direction and at heights of 50, 250, and 500 m and every 500 m thereafter up to 10 km AGL. In total, 873 separate forward trajectories are analyzed. The paths of the forward trajectories and the  $\theta_e$  values along these trajectories are shown in three-dimensional space in Fig. 4. The average sounding through the trajectory curtain is shown in Fig. 5. The environment is nearly saturated below 600 hPa and the temperature profile is close to the moist adiabatic lapse rate, as is often observed in the tropics.

*d. Backward trajectory initialization*

Backward trajectories are initialized at 0040 UTC (the end of the analysis period) within regions of deep convection above 10 km AGL at the center of grid boxes

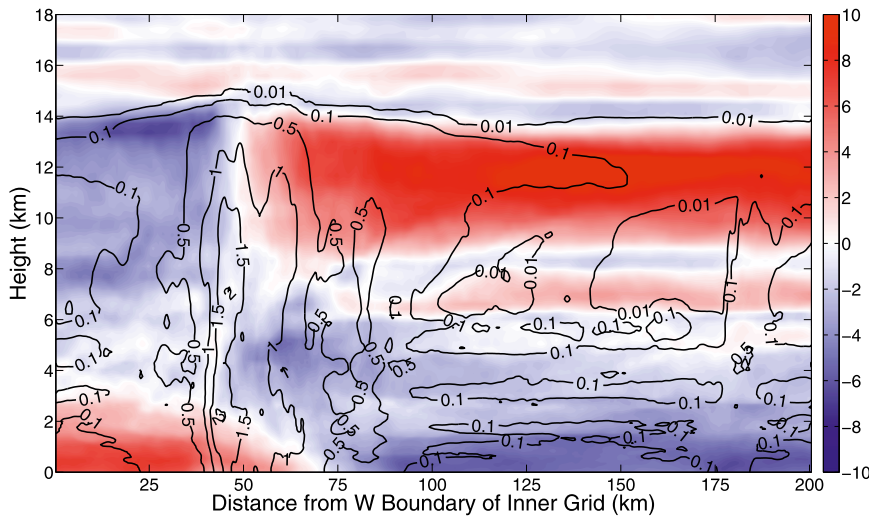


FIG. 2. Inner grid at 2310 UTC: vertical profile of meridionally averaged zonal wind ( $\text{m s}^{-1}$ ; shaded) and meridionally averaged total condensate ( $\text{g kg}^{-1}$ ; black contours).

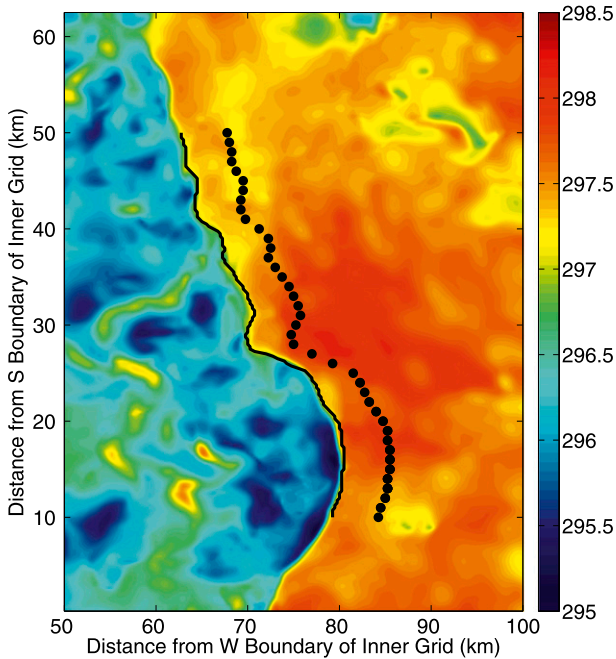


FIG. 3. Surface temperature (K; shaded), locations of forward trajectory origins (black dots), and the gust front defined to be where zonal wind at the surface switches from westerly to easterly (solid black line).

that have total condensate mixing ratios greater than  $0.01 \text{ g kg}^{-1}$ . Trajectories in what is referred to as group A additionally meet the following conditions: 1) they have vertical velocities either greater than  $1 \text{ m s}^{-1}$  or less

than  $-1 \text{ m s}^{-1}$ , and 2) within the vertical grid column where a trajectory is initialized, all grid boxes between the 10-km level and the trajectory initialization location must have velocities that meet the first criterion. Trajectories that are in regions above 10 km AGL where the total condensate mixing ratio is greater than  $0.01 \text{ g kg}^{-1}$ , but that do not meet the aforementioned vertical velocity criteria are placed into what is called group B. This partitioning is designed to differentiate to first order between backward trajectories that end in convective cores (where there are strong updrafts and downdrafts) and those that end in the anvil region (where vertical motions are comparatively weaker). Trajectories within regions contiguous with a vertical velocity maximum greater than  $1 \text{ m s}^{-1}$  or less than  $-1 \text{ m s}^{-1}$  (i.e., above but spatially discontinuous with the 10-km level) are placed into group B. This allows group A to be composed solely of vertical velocity maxima that are sufficiently spatially continuous with lower altitudes to be justified as true convective cores. Group A (group B) trajectories are spaced 2.5 (10) km apart horizontally, and both groups' trajectories are spaced 500 m apart vertically above 10 km AGL within regions where total condensate exceeds  $0.01 \text{ g kg}^{-1}$ . In regions of cloud between 10 km AGL and the cloud top, all grid points are in one group or the other. Below 10 km AGL there are no grid points in either group.

For both the forward and backward trajectories, an offline routine of spatial interpolation, which was successfully applied in Seigel and van den Heever (2012),

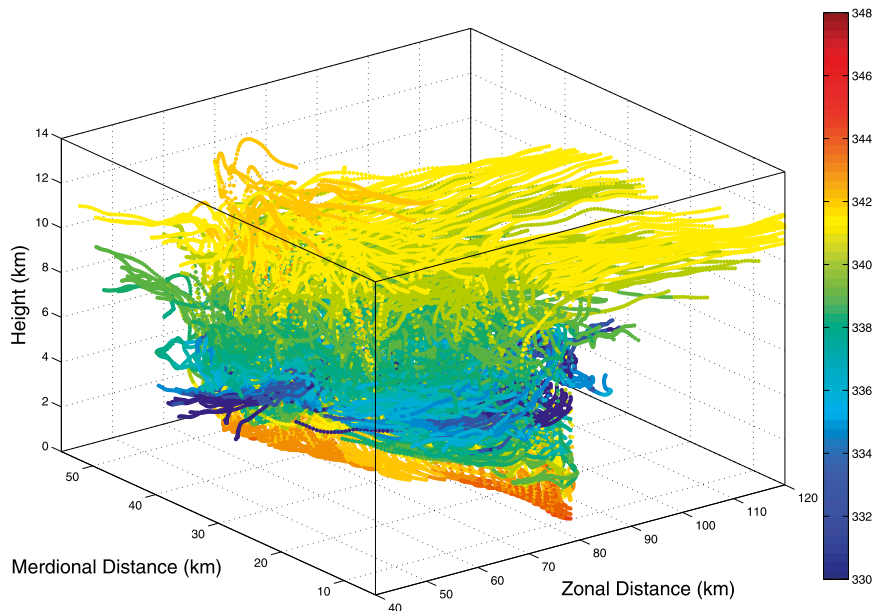


FIG. 4. Paths of forward trajectories, where distances are the distances to the edge of the finer grid.

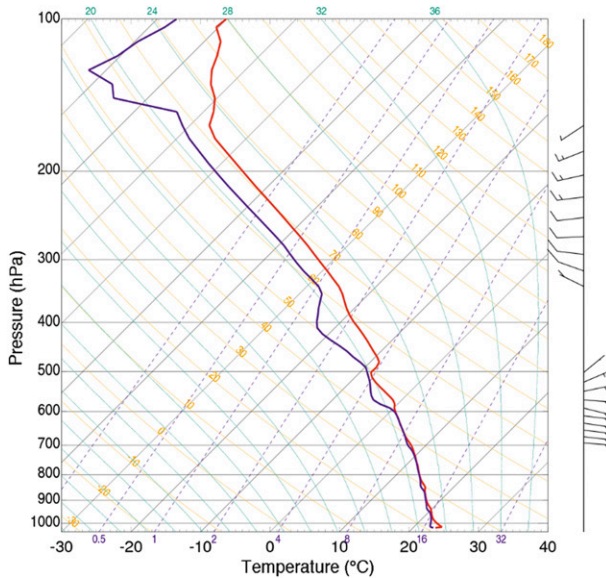


FIG. 5. Average sounding of the profiles from which forward trajectories originate.

is used to facilitate a smooth transition of all variables along trajectories as the trajectories are advected to different grid cells. Trajectories that at any time are within 5 km of the finer grid boundary, are advected out the top of the domain, or are advected below model level 2 are ignored for all analyses described in subsequent sections. As a result, 1233 trajectories are analyzed in group A and 1472 trajectories are analyzed in group B. The same criteria for accepting backward trajectories are applied to the forward trajectories. The following variables are tracked along each trajectory: position, three-dimensional velocity ( $\text{m s}^{-1}$ ), pressure (hPa),  $\theta$  (K),  $\theta_e$  (K), total condensate ( $\text{g kg}^{-1}$ ), vapor mixing ratio ( $\text{g kg}^{-1}$ ), and the mixing ratios ( $\text{g kg}^{-1}$ ) of the mass converted during phase transitions for six latent heating processes, as described in the following section.

### e. Thermodynamic variables

#### 1) LATENT HEATING

To diagnose the latent heating budgets along trajectories in a manner similar to Fierro et al. (2012), microphysical tracking variables within RAMS are utilized at every time step: these are the mass mixing ratios involved with phase transitions for specific microphysical processes, including 1) cloud nucleation, 2) condensation–evaporation, 3) vapor deposition–sublimation, 4) riming of cloud water, 5) freezing of rainwater, and 6) melting. These mass mixing ratios are converted into latent heating and cooling rates. Although the latent heat of vaporization and latent heat of fusion vary with temperature,

constants are used for these two quantities since RAMS uses constants for these variables online as the simulation evolves. Of all the microphysical processes listed above, only the riming of cloud water, the freezing of rainwater, melting, and the liquid–ice portion of vapor deposition–sublimation can change  $\theta_e$ , since release or absorption of the latent heat of vaporization cannot change  $\theta_e$ .

#### 2) EQUIVALENT POTENTIAL TEMPERATURE

This study uses the pseudoadiabatic formulation for equivalent potential temperature not conserved for ice processes put forward by Bolton (1980). Temperature changes associated with water and ice loading along the parcel trajectory are ignored with the Bolton formulation; however, this form is appropriate for the tropical atmosphere to the extent that the warm rain process is very efficient in the tropics and condensate is rapidly rained out of convective storms. Following a trajectory,  $\theta_e$  is conserved during dry motion, condensation, and evaporation, but  $\theta_e$  changes because of mixing, radiative effects, and latent heating–cooling due to ice processes. The change in  $\theta_e$  along a trajectory between two temporally adjacent time steps  $t$  and  $t + 1$  can therefore be approximated using Eq. (1):

$$\Delta\theta_e \approx \frac{L_v}{c_p} \frac{\theta_e^t}{T^t} (\text{ICE}^t) + \text{mixing}^t + \text{radiation}^t, \quad (1)$$

where  $\Delta\theta_e = \theta_e^{t+1} - \theta_e^t$ , the first term on the RHS is the change in  $\theta_e$  due to latent heating–cooling from ice processes, and the second and third terms are changes in  $\theta_e$  due to mixing and radiative processes, respectively. The scale factor of  $\theta_e/T$  is an approximation that assumes the ratio of  $\theta_e$  to  $T$  remains constant in one time step. Since  $\Delta\theta_e$  is evaluated very frequently (on the model time step of 3 s), this approximation appears to be reasonable. After calculating  $\theta_e$  at every time step along each trajectory using the Bolton (1980) form,  $\Delta\theta_e$  is calculated as shown above. Subtracting the latent heating due to ice processes from  $\Delta\theta_e$  leaves mixing and radiation as a combined residual term.

For the sake of model runtime efficiency, radiative tendencies are only updated every 20 min; this time scale is too infrequent to allow an accurate diagnosis of radiative heating rates along trajectories ascending rapidly through an updraft. However, latent heating dominates radiative heating by several orders of magnitude throughout most of the finer grid. Figure 6a shows the ratio of the absolute value of total latent heating to the absolute value of total radiative heating rate for the outer grid, with the finer nested grid highlighted in the translucent

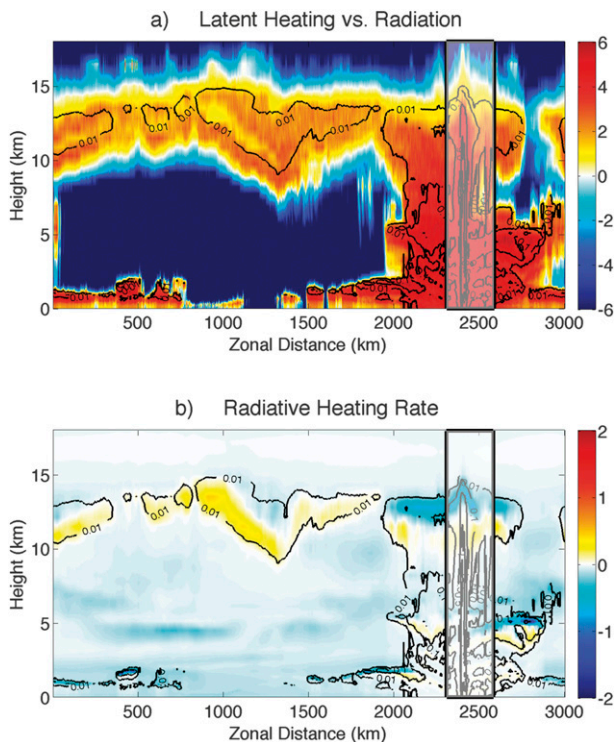


FIG. 6. (a) Meridionally averaged cross section at 2310 UTC; shading represents the unitless ratio between the absolute value of total latent heating rate ( $\text{K h}^{-1}$ ) and the absolute value of the heating rate ( $\text{K h}^{-1}$ ) for all radiative processes, shown on a log scale [e.g., values of +2 (−2) indicate latent heating being two orders of magnitude larger (smaller) than radiative heating]. Translucent boxes indicate the location of the finer grid. Warm (cool) colors indicate where latent heating is larger (smaller) than radiation. Contours indicate meridionally averaged total condensate ( $\text{g kg}^{-1}$ ). (b) As in (a), but shaded contours are meridionally averaged radiative heating rate ( $\text{K h}^{-1}$ ).

white box. In most of the outer grid, which is characterized by clear air, radiative heating dominates latent heating. But inside the fine grid, where there is more active convection, latent heating greatly exceeds radiative heating. Even at cloud top on the fine grid, where radiative heating becomes more important, the total radiative heating rates do not exceed  $2 \text{ K h}^{-1}$  (Fig. 6b). Therefore, the effects of radiation on  $\theta_e$  are treated as negligible, and the along-trajectory change in  $\theta_e$  not explained by latent heating–cooling due to ice processes is understood to be an approximate representation of mixing. The equation for  $\Delta\theta_e$  shown in (1) is therefore modified to the form shown in Eq. (2), where the negligible radiative contributions are implicitly included within the mixing term

$$\Delta\theta_e \approx \frac{L_v \theta_e^t}{c_p T^t} (\text{ICE}^t) + \text{mixing}^t. \quad (2)$$

### 3. Results

#### a. Forward trajectories

The forward trajectories, which start in a curtain in front of the convection, ascend to various heights during the simulation. Figures 7a and 7b show the maximum heights achieved by these trajectories and the maximum amount of descent experienced by trajectories, respectively, as a function of trajectory starting altitudes. Figure 7a illustrates that trajectories that begin close to the surface are more likely to reach the upper troposphere than trajectories that begin in the middle troposphere. For example, 51.2% (80.5%) of trajectories that begin 50 m AGL ascend higher than 10 (8) km AGL, while 9.8% (17.1%) of trajectories that begin 5 km AGL ascend higher than 10 (8) km AGL. Fierro et al. (2012) showed a similar percentage of near-surface trajectories reaching above 10 km AGL [46.7% in Fierro et al. (2012) versus 51.2% in this study]. This agreement is perhaps not surprising, since maximum updraft intensities and horizontal grid spacing are comparable between this study and Fierro et al. (2012). Mechem et al. (2002) showed a qualitative agreement with the maximum height distribution in Fig. 7a in that fewer trajectories originating from around the midtropospheric  $\theta_e$  minimum reached the upper troposphere than those starting from near the surface in higher- $\theta_e$  air. Trajectories that begin above 8 km are very likely to reach above 10 km AGL simply by virtue of having a limited vertical distance to travel. Figure 7b demonstrates that trajectories beginning at midlevels tend to descend more than those beginning near the surface; for example, none of the trajectories starting below 2 km AGL are at any height lower than 250 m below their initial height, while 75.6% (53.7%) of trajectories starting at 5 km AGL descend at least 250 (500) m below their initial height. The statistics in Fig. 7b are qualitatively consistent with the crossover zone model in Zipser (1977) in that air in the near-storm environment originating from above the subcloud layer is more likely to descend upon interacting with the convection than air in the near-storm environment originating from below the subcloud layer. The crossover zone model also allows for some inflow from above the subcloud layer to ascend within the convection (Zipser 1977), since air from the subcloud layer is likely to mix to some degree with the air beginning above cloud base. This mixing was seen in Mechem et al. (2002) and is also observed in this study, as evidenced by the nonnegligible number of trajectories of midlevel origin that are able to ascend to the upper troposphere. The above discussion shows notable ways in which the crossover zone model is supported by the results of this study.

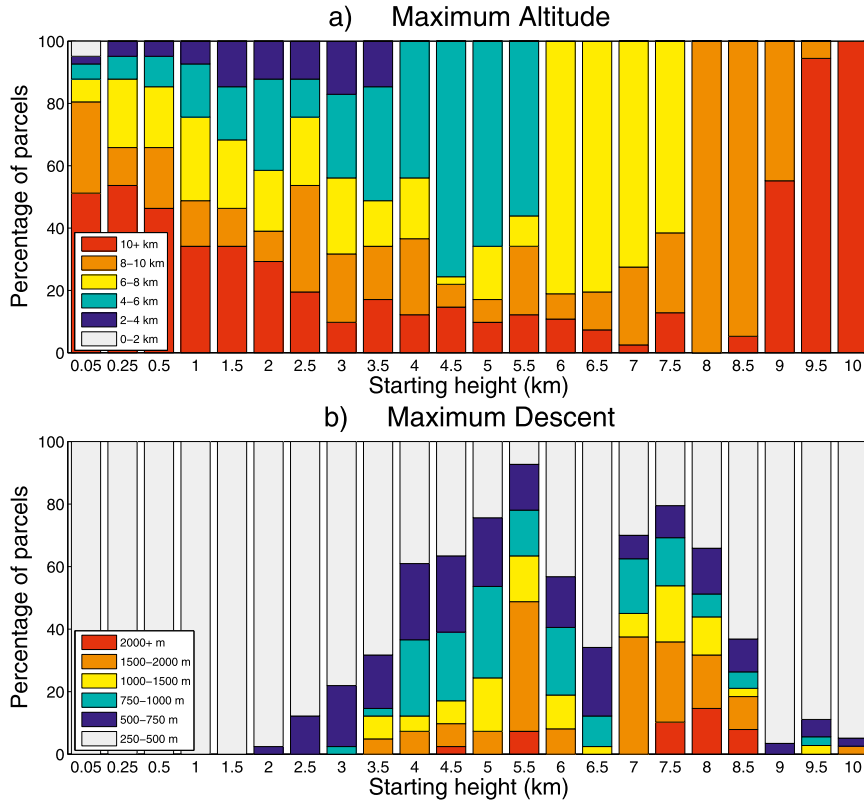


FIG. 7. Distributions for forward trajectories based on starting altitude of (a) maximum heights achieved and (b) maximum amount of descent experienced.

However, unlike what would be expected by the crossover model, trajectories of midlevel origin are more likely to rise than sink upon interacting with the convection in this simulation. For the trajectories starting between 4 and 6 km AGL, there is a longer tail in the distribution of upward motion than for downward motion (not shown). Thus, although the results in this study are consistent with the crossover zone in the qualitative sense that trajectories originating from the lower- $\theta_e$  layers above the subcloud layer are more likely to descend than their near-surface counterparts upon interacting with the convection, the absolute number of rising trajectories from the lower- $\theta_e$  layers is still higher than the number of descending trajectories from those layers. The tendency in this study for a majority of trajectories originating from all inflow layers to rise upon interacting with the convection may be related to the moist nature of the entire depth of the troposphere, as shown in the sounding in Fig. 5. The moist environment in this study is similar to the environment in Mechem et al. (2002) with higher midlevel relative humidity, and is also similar to their simulations with moister middle levels in terms of the difference in the  $\theta_e$  values between the surface and the middle troposphere. Both moist simulations in

Mechem et al. (2002) showed a higher percentage of midlevel parcels ascending to the upper troposphere within the convective updrafts than their drier simulation. They attributed this to the midlevel inflow in the moister simulations saturating more quickly than the midlevel inflow in the drier simulation upon interacting with the convection.

*b. Backward trajectories*

1) HEIGHTS

Figure 8 illustrates the height distribution of the backward trajectories. At the end of the simulation, when the backward trajectories are initialized (0040 UTC; Fig. 8a), group A and group B trajectories are both above 10 km AGL, as described in section 2. Ten minutes prior to the end of the simulation (0030 UTC; Fig. 8b), nearly half of the group A trajectories are below 10 km AGL, with a small number below 5 km. Most of the group B trajectories remain above 10 km. Fifty minutes before the end of the simulation (2350 UTC; Fig. 8c), group A trajectories are relatively evenly distributed throughout the troposphere, while group B trajectories are still predominantly confined to above 10 km. At the

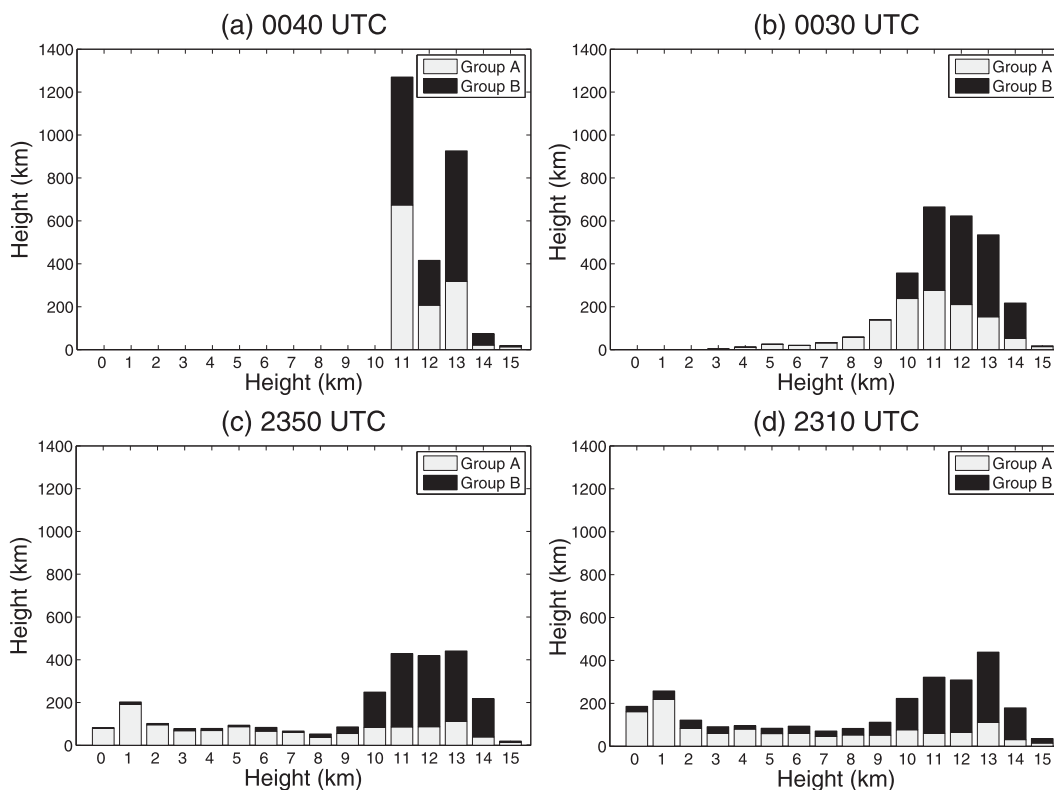


FIG. 8. Histograms of backward trajectory heights (group A in gray, group B in black) at (a) 0040 UTC when backward trajectories are initialized, all above 10 km AGL; (b) 0030 UTC; (c) 2350 UTC; and (d) 2310 UTC, which is the initial time of the simulation.

start of the simulation (2310 UTC; Fig. 8d), some of the group B trajectories are spread through the lower and middle troposphere, but most still remain above 10 km. There is very little change in the height distributions of both trajectory groups in the first hour of the simulation; most of the vertical motion within convective updrafts for both groups occurs in the last half hour.

Since group A trajectories are defined as those within stronger updrafts and downdrafts contiguous with the 10-km level, it is not surprising that many more group A than group B trajectories have their origin in the lower and middle troposphere. Sixty-six percent of the group A trajectories that are analyzed have their origin above 2 km AGL at 2310 UTC. For group B trajectories that are analyzed, 94% have their origin above 2 km AGL at 2310 UTC. These results may appear to be in contradiction with the results from the forward trajectories, since a higher percentage of forward trajectories originating from near the surface were able to ascend to above 10 km AGL compared with forward trajectories starting at midlevels. This supposed contradiction is likely due to how the backward trajectories were defined; the vertical velocity threshold is meant to separate groups A and B into regions of stronger and weaker

vertical motions at the initiation time of 0040 UTC, respectively, but the exact cutoff value between groups A and B of  $\pm 1 \text{ m s}^{-1}$  is arbitrary.

It is useful to stratify the group A backward trajectories based on vertical velocity at 0040 UTC to see if there is a relationship between the trajectories' vertical velocities at 0040 UTC and their corresponding heights at 2310 UTC. The group A backward trajectories are therefore subdivided into bins of vertical velocity at their initiation time of 0040 UTC that have values of  $< -4$ ,  $-4$  to  $-2$ ,  $-2$  to  $0$ ,  $0$  to  $2$ ,  $2$  to  $4$ ,  $4$  to  $6$ ,  $6$  to  $8$ ,  $8$  to  $10$ , and  $> 10 \text{ m s}^{-1}$ . The number of trajectories in each bin is recorded, and the percentage of trajectories within each bin that are below 2 km AGL at the beginning of the simulation (2310 UTC) is calculated. Figure 9 illustrates the results. Group A backward trajectories with stronger upward motion at 0040 UTC are more likely to originate in the lowest 2 km above the surface than the group A backward trajectories with weaker upward motion or downward motion at 0040 UTC. This makes sense given that near-surface inflow trajectories have higher initial  $\theta_e$  than their midlevel counterparts; hence, near-surface trajectories are likely more positively buoyant and therefore more likely to occupy

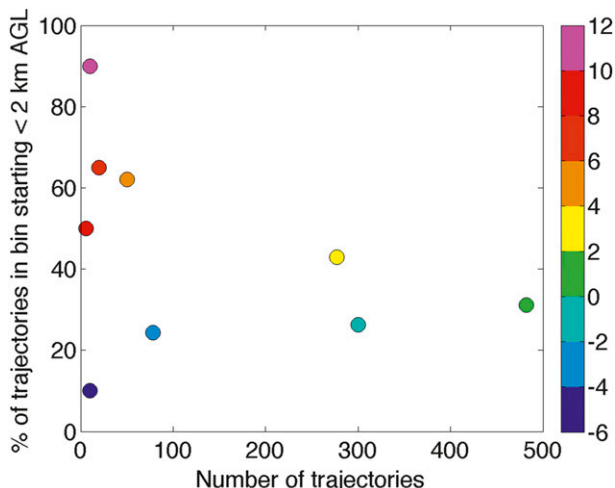


FIG. 9. Number of group A trajectories having vertical velocities at 0040 UTC within the range indicated in the color table, and the percentage of the trajectories in each velocity bin that start below 2 km AGL.

the strongest updrafts. At the same time, midlevel inflow is being entrained into the convection and ascending to the upper troposphere as well, albeit more slowly than the trajectories of near-surface origin. This indicates that the midlayer inflow is not as likely to be entrained into the center of the updrafts but can still ascend to the upper troposphere. Inflow over a large depth of the troposphere appears to be important in these simulations.

## 2) LATENT HEATING CHANGES

Since group A has more trajectories that represent lower and middle tropospheric convective inflow than group B, the most detailed analyses of latent heating and mixing in the remainder of this study will be focused on group A. The microphysical processes contributing to latent heating along the group A trajectories throughout the simulation are shown in Fig. 10, binned as a function of the trajectories' height at 2310 UTC (the beginning of the analysis period) and height at any later time. It should be emphasized that the values shown in Fig. 10 are averages, and therefore do not reflect the extremes of latent heating rates along individual trajectories. Figures for cloud nucleation (Fig. 10a), condensation and evaporation (Fig. 10b), freezing of condensate (Fig. 10c), deposition and sublimation (Fig. 10d), and melting (Fig. 10e) are shown. Group A trajectories have ice nucleation heating rates greater than  $1 \text{ K h}^{-1}$  only 0.04% of the time; therefore, ice nucleation is not shown. The solid black line on the plots indicates where the initial height equals the height at any later time. In general, trajectories that start at lower initial heights have higher

latent heating rates for all processes, although this is particularly true for cloud nucleation and condensation.

Cloud nucleation and condensation both contribute to latent heating significantly up to approximately 6 km AGL, with average heating rates peaking at about 5 km. Heating rates from cloud nucleation exceed  $80 \text{ K h}^{-1}$  and heating rates from condensation reach  $40 \text{ K h}^{-1}$ . Evaporation along ascending trajectories within updrafts is localized in the one to two model levels above the top edge of where condensation occurs, resulting in a cooling rate due to evaporation that averages  $10 \text{ K h}^{-1}$  around 7 km AGL. These one to two model levels are also where vapor deposition onto ice first becomes strongly positive in the vertical and where the vapor pressure is greater than (less than) the saturated vapor pressure with respect to ice (water) (not shown). The loss of liquid water around 7 km AGL is thus evidence of the Wegener–Bergeron–Findeisen process. Cooling rates due to melting are generally between 5 and  $10 \text{ K h}^{-1}$  in the 2 km below the freezing level and are highest for trajectories that begin in the lowest 2 km AGL. Above the freezing level, both the freezing of condensate and vapor deposition onto ice contribute to latent heating. Condensate freezing predominantly occurs just above the freezing level; at 2310 UTC, 33.9% of freezing occurs at temperatures below  $-5^\circ\text{C}$ , 6.2% occurs below  $-10^\circ\text{C}$ , and just 1.0% occurs below  $-15^\circ\text{C}$ . The amounts of supercooled water as a function of temperature for observations in Stith et al. (2002) agree well with the freezing percentages as a function of temperature observed in this study. Condensate freezing has heating rates just over  $10 \text{ K h}^{-1}$  between 4 and 7 km AGL for trajectories of near-surface origin; these heating rates are nearly an order of magnitude smaller than the heating rates due vapor deposition, which sometimes exceed  $100 \text{ K h}^{-1}$  and occur between 6.5 and 12 km AGL.

The effect of vapor being deposited onto all ice species may be more important than the freezing of rainwater in providing latent heating in tropical deep convection. The dominant role of vapor deposition compared to freezing is supported by the modeling study of Johnson et al. (2002) and stands in contrast to the results offered by Fierro et al. (2012) (both of which used 1M schemes), who showed heating rates from condensate freezing of  $300 \text{ K h}^{-1}$  and heating rates from vapor deposition of  $20 \text{ K h}^{-1}$ . The microphysical scheme used here does not assume that cloud droplets are monodisperse in size or that rainwater freezes instantaneously above the freezing level, which were assumptions in the microphysical scheme used by Fierro et al. (2012). These assumptions may have had a large effect on the vertical profile of latent heating in Fierro et al. (2012). Therefore, the absence of these assumptions in the RAMS microphysical scheme

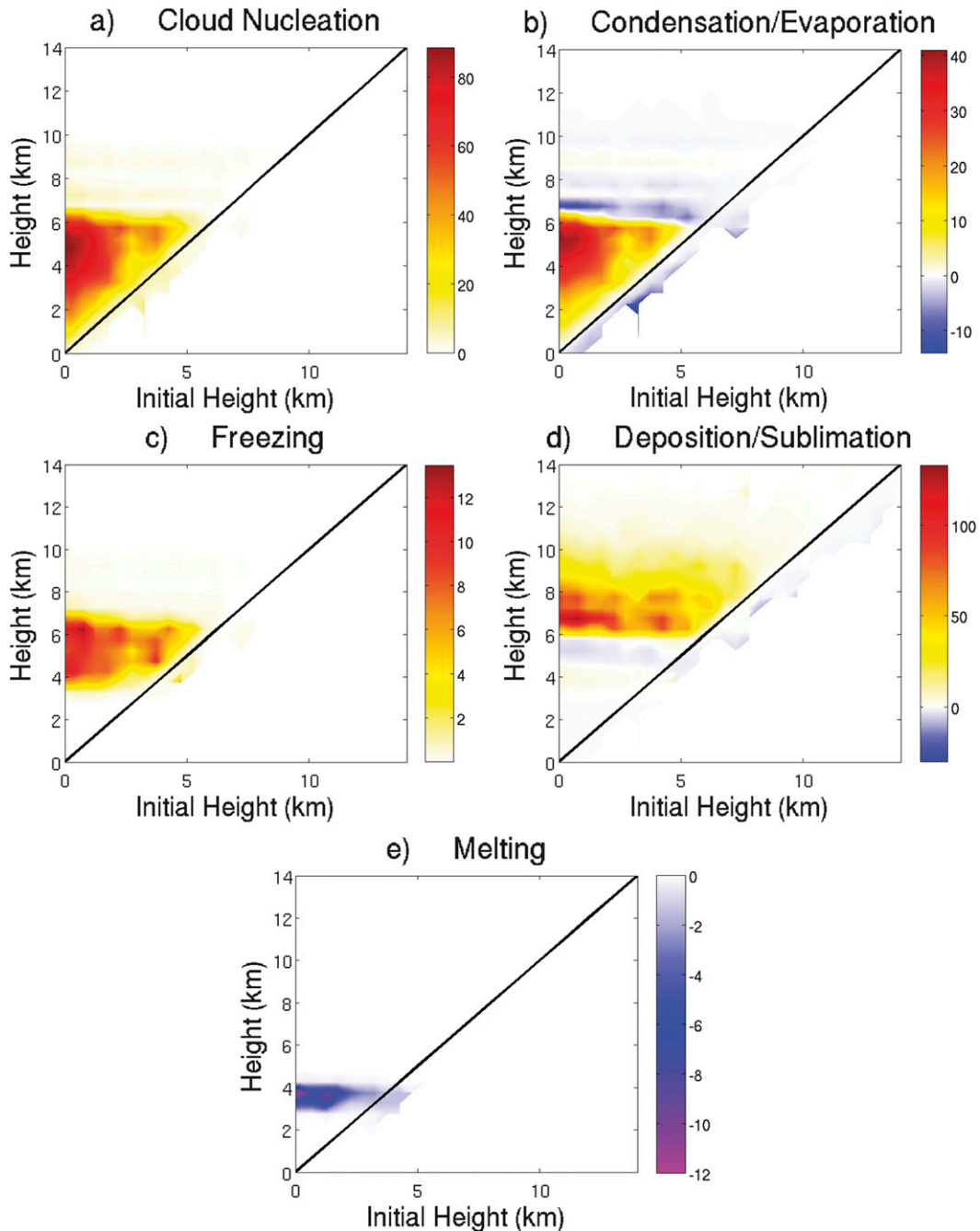


FIG. 10. Mean heating-cooling rates associated with (a) cloud nucleation, (b) condensation-evaporation, (c) freezing of condensate, (d) deposition-sublimation, and (e) melting within RAMS, where colors are the mean heating-cooling rates for these processes. Heating-cooling rates are binned as a function of initial height and current height. Heating rates are positive and cooling rates are negative. Solid line is where initial height equals current height.

lends confidence to the relative amounts of freezing of condensate and vapor deposition observed in this study.

Vapor deposition releases the latent heat of fusion, but it also releases the latent heat of vaporization. The

portion of vapor depositional latent heating due to the latent heat of vaporization cannot change  $\theta_e$ . As a result, despite the fact that the magnitude of the latent heat released by vapor deposition is roughly an order of magnitude greater than the latent heat released by the

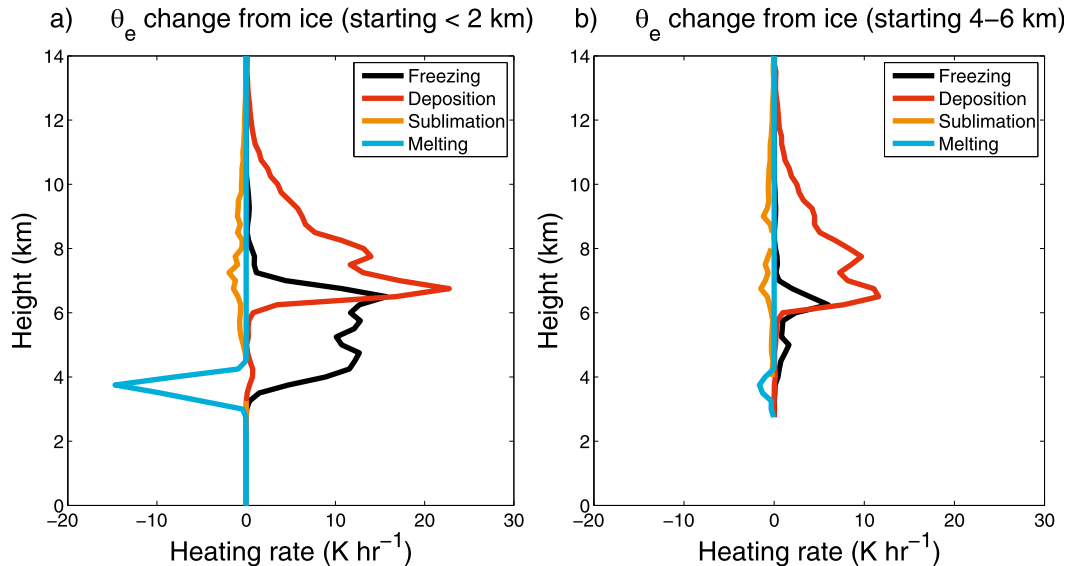


FIG. 11. The rate at which  $\theta_e$  changes ( $\text{K h}^{-1}$ ) along group A backward trajectories that at 2310 UTC are (a) below 2 km AGL and (b) between 4 and 6 km AGL, each partitioned by freezing, deposition, sublimation, and melting. The choice of these two layers facilitates a first-order comparison of latent heating and mixing between near-surface inflow and midlevel inflow.

freezing of condensate, the freezing of condensate changes  $\theta_e$  by roughly the same order of magnitude as vapor deposition for trajectories starting in the lowest 2 km (Fig. 11a). For group A backward trajectories starting between 4 and 6 km AGL (Fig. 11b), vapor deposition onto ice changes  $\theta_e$  more than freezing of condensate owing to the many trajectories starting above the level of the maximum freezing of condensate.

### 3) EQUIVALENT POTENTIAL TEMPERATURE CHANGES

Because of the limited magnitudes of the radiative heating rates in deep convection, changes to  $\theta_e$  along the group A backward trajectories can be partitioned into contributions from latent heating due to ice processes and mixing, as described in section 2. For the remainder of the paper, the ice latent heating-cooling term is referred to as LAT and the residual term as RES. A positive (negative) value of RES along a trajectory means that the trajectory is mixing with higher (lower)- $\theta_e$  air. Figures 12a and 12b illustrate the average of LAT as a function of height and  $\theta_e$  at any time; Figs. 12c and 12d show the average of RES in the same manner. Figures 12e and 12f show the average LAT+RES. Figures 12g and 12h show the contoured frequency by altitude diagram (CFAD) of  $\theta_e$ , which both demonstrate that the vast majority of trajectories have  $\theta_e$  values greater than the environmental  $\theta_e$  profile. Figures 12i and 12j show the average vertical velocity. The black curve represents the average  $\theta_e$  within columns occupied by group A

trajectories at 2310 UTC and is representative of the near-storm environment. For each pair of plots, trajectories starting between the surface and 2 km AGL and between 4 and 6 km AGL are shown. These levels are chosen because they facilitate a first-order comparison between trajectories that start near the surface in high- $\theta_e$  air and those that start in the middle troposphere where  $\theta_e$  is near its profile minimum.

Latent heating due to ice processes and mixing are first examined for trajectories that begin in the lowest 2 km AGL. RES is slightly negative (up to  $-5 \text{ K h}^{-1}$ ) from the surface to 4 km (Fig. 12c) and LAT is also negative, with rates of about  $-10 \text{ K h}^{-1}$  around 1 km below the freezing level (Fig. 12a). RES is negative whenever a parcel trajectory mixes with drier and/or cooler environmental air (where the term “environmental” is taken to mean “outside the cloudy updraft”) or when a parcel trajectory mixes with air in the cloudy updraft that is drier and/or cooler. Mixing with environmental air is likely associated with entrainment of cooler and/or drier air, while a reduction in  $\theta_e$  due to mixing within the updraft is likely due to the parcel entering a region where the amount of latent heating due to ice processes (LAT) is positive but decreasing along the trajectory.

Since the environmental profile of  $\theta_e$  decreases strongly with height in the lower troposphere and LAT is zero in the lower troposphere, the negative RES values at these heights indicate reductions in  $\theta_e$  due to entrainment of drier and/or cooler air. Above the melting level ( $\sim 4.6 \text{ km}$ )

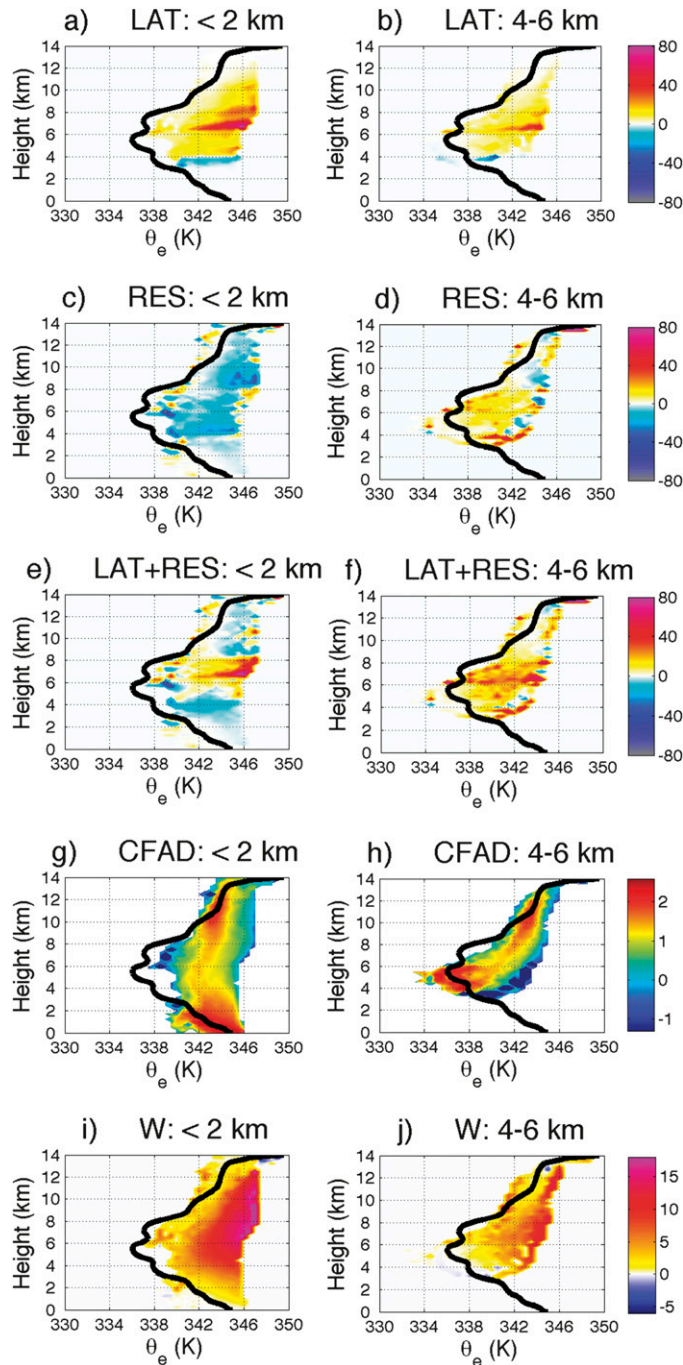


FIG. 12. Average latent heating due to ice processes along group A trajectories that at 2310 UTC are (a) below 2 km AGL and (b) between 4 and 6 km AGL, average residual heating rate along group A trajectories that at 2310 UTC are (c) below 2 km AGL and (d) between 4 and 6 km AGL, average latent heating due to ice processes plus the residual heating rate along group A trajectories that at 2310 UTC are (e) below 2 km AGL and (f) between 4 and 6 km AGL, CFAD of number of group A trajectories (expressed as  $\log_{10}$  of the number of observations, converted to minutes) that at 2310 UTC are (g) below 2 km AGL and (h) between 4 and 6 km AGL, and average vertical velocity ( $\text{m s}^{-1}$ ) of group A trajectories that at 2310 UTC are (i) below 2 km AGL and (j) between 4 and 6 km AGL, black curve represents average  $\theta_e$  of all group A trajectories at that level at 2310 UTC.

it is likely that entrainment of drier and/or cooler air is still present, since environmental  $\theta_e$  values are significantly lower than parcel  $\theta_e$  values in the middle and upper troposphere. However, in regions above the melting level where LAT is both positive and decreasing in magnitude with height along ascending trajectories, negative RES values may also indicate mixing with cooler (and possibly drier) air within the updraft. Regardless of whether RES is negative due to the trajectories' mixing with drier and/or cooler environmental air or lower- $\theta_e$  air in the cloudy updraft, it is clear that from 6 to 9 km LAT becomes strongly positive such that it more than cancels the negative RES at these levels (Fig. 12e). Thus, the general narrative of what changes  $\theta_e$  along parcels ascending from near the surface is similar to what has been concluded previously in other studies (Zipser 2003; Fierro et al. 2009, 2012; Romps and Kuang 2010). For these trajectories of near-surface origin,  $\theta_e$  decreases in the lower troposphere owing to entrainment-induced cooling and increases in the middle and upper troposphere owing to ice processes.

The magnitudes of the latent heating due to condensate freezing are smaller in this study compared with Fierro et al. (2012). The major consequence of this difference is that  $\theta_e$  along trajectories does not increase significantly in this study until ascending above about 6 km AGL, which is where both freezing of condensate and vapor deposition are both contributing to latent heating; between 4 and 6 km, cooling and drying likely due to entrainment are large enough to balance the latent heating from the freezing of condensate (Fig. 12e), resulting in little  $\theta_e$  change at these levels. This result, which applies to trajectories of near-surface origin, illustrates that latent heating must be larger than the cooling due to entrainment in order for  $\theta_e$  to increase along trajectories.

Trajectories that begin between 4 and 6 km AGL are now discussed. LAT is maximized at the same heights as trajectories that ascend from the lowest 2 km AGL, but the magnitudes are smaller (Fig. 12b). Negative LAT values in the melting layer are also less pronounced since most of the trajectories, which are predominantly ascending, begin above that level. RES is positive throughout most of the troposphere, particularly between 3 and 8 km AGL (Fig. 12d). As these trajectories are entrained into the convection from the drier midlevel environment, they mix with higher  $\theta_e$  air of the convective cores, causing the positive RES response. Thus, the combined effect of LAT+RES is strongly positive, even at levels vertically well away from the latent heating maximum (Fig. 12f). As these midlevel trajectories acquire the properties of the updrafts that entrain them, the updraft itself must become diluted.

This is reflected in the negative midlevel RES values for trajectories ascending from the lowest 2 km (Fig. 12c). The vertical velocities of the trajectories of midlevel origin are not as strong as those that ascend from near the surface (Figs. 12i,j). It should be noted that Figs. 12a–f, 12i, and 12j display average values; for example, this means that vertical velocities along trajectories (Figs. 12i,j) are not always positive in the upper troposphere. Consistent with the other findings of this study, the entrained midlevel trajectories may not be buoyant enough to support the strongest updrafts.

To test whether the results of this study are sensitive to which trajectory group is analyzed, plots analogous to those in Fig. 12 (corresponding to LAT, RES, and vertical velocity, respectively) were produced for all group B backward trajectories and all forward trajectories (not shown). Although there are quantitative differences between among the trajectory groups, they are strongly similar qualitatively despite differences in where they are initialized. The results of this study thus appear to be qualitatively insensitive to the location of trajectory initialization.

#### 4. Conclusions

Studies in recent years have modified the HTH first proposed by Riehl and Malkus (1958) toward an understanding that latent heating due to ice processes is sufficient to drive convective towers to the upper troposphere, despite environmental dilution (Zipser 2003; Fierro et al. 2009, 2012). Through Lagrangian trajectory analysis in an idealized, high-resolution CRM simulation of tropical deep convection that is approaching radiative–convective equilibrium, this study builds on the findings of Fierro et al. (2009, 2012) by using a more sophisticated two-moment microphysical scheme. This study focuses on the mature stage of a simulated tropical deep convective system organized into a line of cells; thus, the results of this study are not necessarily representative of all organizational modes or life stages of deep tropical convection.

The first goal of this study was to analyze the microphysical processes that contribute to latent heating in deep convection. Latent heating along ascending trajectories comes primarily from cloud nucleation and condensation between the surface and 6 km. Within the lower and middle troposphere, cloud nucleational heating rates peak at about  $80 \text{ K h}^{-1}$  and condensational heating rates maximize at about  $40 \text{ K h}^{-1}$ . Above the freezing level, which is at approximately 4.6 km AGL, the riming of cloud water and freezing of rainwater contribute to latent heating up to 7 km AGL and contribute a combined  $8\text{--}12 \text{ K h}^{-1}$  for most trajectories ascending

from the lowest 2 km. Between 6 and 12 km, the heating rates from vapor deposition onto ice dominate the total latent heating rate, which frequently exceeds  $40 \text{ K h}^{-1}$  and sometimes reaches over  $100 \text{ K h}^{-1}$  between 6 and 8 km. Cooling rates due to melting near the freezing level are generally low, averaging around 5 to  $10 \text{ K h}^{-1}$  for trajectories originating near the surface. For all microphysical processes, the magnitude of the latent heating–cooling decreases as the initial height of the trajectory increases. This is particularly true for cloud nucleation and condensation.

The second goal was to assess causes of  $\theta_e$  change along trajectories. Along trajectories, radiative heating rates are shown to be much smaller than latent heating rates, which means that  $\theta_e$  changes primarily because of latent heating from ice processes, or mixing with either higher- or lower- $\theta_e$  parcels. For trajectories starting in the lowest 2 km, the entrainment of drier and/or cooler air causes  $\theta_e$  to decrease below the freezing level. Notably, cooling rates due to mixing are larger above the freezing level than below the freezing level. Between 4 and 6 km AGL, latent heating due to the freezing of condensate are exceeded by the cooling due to mixing. Above 6 km, cooling and/or drying due to mixing remains substantial, but the latent heating due to vapor deposition becomes enough to offset the cooling–drying and causes  $\theta_e$  to increase. Above the freezing level, the relative contribution of the freezing of condensate to latent heating is approximately an order of magnitude less than vapor deposition onto ice; this is related to the fact that the latent heat of sublimation is an order of magnitude greater than the latent heat of fusion. However, since the latent heat of fusion is the only contributor to  $\theta_e$  change, it turns out that freezing processes have approximately the same combined effect on  $\theta_e$  as vapor deposition onto ice. This result stands in contrast to the relative importance of vapor deposition in changing  $\theta_e$  as identified in Fierro et al. (2012); they showed that freezing processes caused  $\theta_e$  to increase by nearly an order of magnitude more than vapor deposition onto ice, perhaps in part because of the assumptions in their microphysical scheme that rainwater freezes instantaneously above the freezing level or that cloud droplets are monodisperse in size. The microphysical scheme used in this study thus lends confidence to the results presented herein. The results of this study uphold a general narrative supported by Zipser (2003), Fierro et al. (2009), Romps and Kuang (2010), and Fierro et al. (2012)—namely, that  $\theta_e$  decreases in the lower troposphere owing to entrainment cooling and increases in the middle and upper troposphere owing to ice processes. Advancements within this study are the explicit quantification of the residual cooling due to

mixing (which may be largely due to entrainment of cooler and/or drier air) above the freezing level, and finding the source heights of convective inflow throughout the depth of the troposphere.

Trajectories starting between 4 and 6 km AGL have latent heating profiles qualitatively similar to those starting in the lowest 2 km AGL, with the main exception being that trajectories starting between 4 and 6 km AGL do not experience as much latent heating from condensation, cloud nucleation, or the freezing of condensate, since these processes predominantly occur below the levels at which these midlevel trajectories are mixed into the updraft. Residual rates that change  $\theta_e$  are positive since these trajectories are being entrained into the higher- $\theta_e$  cloudy region or updraft. Well above the freezing level, mean vertical velocities are somewhat diminished compared to trajectories starting in the lowest 2 km; this could indicate that midlevel trajectories exist on the peripheries of updrafts or that they are not buoyant enough to drive the strongest updrafts.

The final goal was to determine the relative roles of near-surface and elevated inflow in the latent heating of deep convection. Although the strongest updrafts are composed of air of near-surface origin, most of the air that is lifted by convective updrafts to above 10 km AGL comes from above the lowest 2 km AGL. Latent heating rates along trajectories originating from the middle troposphere are smaller than their near-surface counterparts but are not insubstantial. This underscores the importance of deep-layer inflow in the simulated deep convection despite the inability of midlevel trajectories to penetrate the strongest updrafts. The results of this study showing a significant role of midlevel inflow are consistent with Mechem et al. (2002), which underscored the importance of deep-layer inflow in moist environments. Particularly within moist environments, such as in this study, Lagrangian trajectory studies of deep convection should ideally analyze inflow from both the lower and middle troposphere. Some convective parameterization schemes rely only on the characteristics of near-surface air for convective inflow. This study and the Mechem et al. (2002) study have both shown that tropical deep convection in its mature stage can draw on inflow from all levels. Therefore, having some representation of deep-layer inflow in all GCM cumulus parameterizations would seem to be a positive step.

*Acknowledgments.* Special thanks are extended to Matthew Igel for providing the original outer grid RCE simulation data. Steve Saleeby is also thanked for providing the microphysical budgeting code within RAMS,

which was critical in diagnosing the latent heating budgets. This work was funded by NASA Grant NNX10AM316. The comments from three anonymous reviewers are also appreciated.

## REFERENCES

- Adams-Selin, R. D., S. C. van den Heever, and R. H. Johnson, 2013: Sensitivity of bow-echo simulation to microphysical parameterizations. *Wea. Forecasting*, **28**, 1188–1209.
- Anderson, N. F., C. A. Grainger, and J. L. Stith, 2005: Characteristics of strong updrafts in precipitation systems over the central tropical Pacific Ocean and in the Amazon. *J. Appl. Meteor.*, **44**, 731–738.
- Betts, A. K., 1976: The thermodynamic transformation of the tropical subcloud layer by precipitation and downdrafts. *J. Atmos. Sci.*, **33**, 1008–1020.
- Bolton, D., 1980: The computation of equivalent potential temperature. *Mon. Wea. Rev.*, **108**, 1046–1053.
- Bryan, G. H., and J. M. Fritsch, 2000: Moist absolute instability: The sixth static stability state. *Bull. Amer. Meteor. Soc.*, **81**, 1207–1230.
- , J. C. Wyngaard, and J. M. Fritsch, 2003: Resolution requirements for the simulation of deep moist convection. *Mon. Wea. Rev.*, **131**, 2394–2416.
- Cotton, W. R., and Coauthors, 2003: RAMS 2001: Current status and future directions. *Meteor. Atmos. Phys.*, **82**, 5–29.
- Dawson, D. T., M. Xue, J. A. Milbrandt, and M. K. Yau, 2010: Comparison of evaporation and cold pool development between single-moment and multimoment bulk microphysics schemes in idealized simulations of tornadic thunderstorms. *Mon. Wea. Rev.*, **138**, 1152–1171.
- Fierro, A. O., J. Simpson, M. A. LeMone, J. M. Straka, and B. F. Smull, 2009: On how hot towers fuel the Hadley cell: An observational and modeling study of line-organized convection in the equatorial trough from TOGA COARE. *J. Atmos. Sci.*, **66**, 2730–2746.
- , E. J. Zipser, M. A. LeMone, J. M. Straka, and J. (Malkus) Simpson, 2012: Tropical oceanic hot towers: Need they be undilute to transport energy from the boundary layer to the upper troposphere effectively? An answer based on trajectory analysis of a simulation of a TOGA COARE convective system. *J. Atmos. Sci.*, **69**, 195–213.
- Gilmore, M. S., J. M. Straka, and E. N. Rasmussen, 2004: Precipitation uncertainty due to variations in precipitation particle parameters within a simple microphysics scheme. *Mon. Wea. Rev.*, **132**, 2610–2627.
- Grabowski, W. W., and M. W. Moncrieff, 2004: Moisture-convection feedback in the tropics. *Quart. J. Roy. Meteor. Soc.*, **130**, 3081–3104.
- Harrington, J., T. Reisin, W. Cotton, and S. Kreidenweis, 1999: Cloud resolving simulations of Arctic stratus: Part II: Transition-season clouds. *Atmos. Res.*, **51**, 45–75.
- Hobbs, P. V., M. K. Politovich, and L. F. Radke, 1980: The structures of summer convective clouds in eastern Montana. I: Natural clouds. *J. Appl. Meteor.*, **19**, 645–663.
- Igau, R. C., M. A. LeMone, and D. Wei, 1999: Updraft and downdraft cores in TOGA COARE: Why so many buoyant downdraft cores? *J. Atmos. Sci.*, **56**, 2232–2245.
- Johnson, D. E., W.-K. Tao, J. Simpson, and C.-H. Sui, 2002: A study of the response of deep tropical clouds to large-scale thermodynamic forcings. Part I: Modeling strategies and simulations of TOGA COARE convective systems. *J. Atmos. Sci.*, **59**, 3492–3518.
- Johnson, R. H., T. M. Rickenbach, S. A. Rutledge, P. E. Ciesielski, and W. H. Schubert, 1999: Trimodal characteristics of tropical convection. *J. Climate*, **12**, 2397–2418.
- Kingsmill, D. E., and R. A. Houze Jr., 1999: Thermodynamic characteristics of precipitating convection over the west Pacific warm pool. *Quart. J. Roy. Meteor. Soc.*, **125**, 1209–1229.
- Lang, S., W.-K. Tao, R. Cifelli, W. Olson, J. Halverson, S. Rutledge, and J. Simpson, 2007: Improving simulations of convective systems from TRMM LBA: Easterly and westerly regimes. *J. Atmos. Sci.*, **64**, 1141–1164.
- , —, X. Zeng, and Y. Li, 2011: Reducing the biases in simulated radar reflectivities from a bulk microphysics scheme: Tropical convective systems. *J. Atmos. Sci.*, **68**, 2306–2320.
- LeMone, M. A., and E. J. Zipser, 1980: Cumulonimbus vertical velocity events in GATE. Part I: Diameter, intensity and mass flux. *J. Atmos. Sci.*, **37**, 2444–2457.
- Lucas, C. E., and E. J. Zipser, 2000: Environmental variability during TOGA COARE. *J. Atmos. Sci.*, **57**, 2333–2350.
- Mechem, D. B., R. A. Houze, and S. S. Chen, 2002: Layer inflow into precipitating convection over the western tropical Pacific. *Quart. J. Roy. Meteor. Soc.*, **128**, 1997–2030.
- Morrison, H., G. Thompson, and V. Tatarskii, 2009: Impact of cloud microphysics on the development of trailing stratiform precipitation in a simulated squall line: Comparison of one- and two-moment schemes. *Mon. Wea. Rev.*, **137**, 991–1007.
- Petersen, W. A., R. C. Cifelli, S. A. Rutledge, B. S. Ferrier, and B. F. Smull, 1999: Shipborne dual-Doppler operations and observations during TOGA COARE. *Bull. Amer. Meteor. Soc.*, **80**, 81–97.
- Pielke, R. A., and Coauthors, 1992: A comprehensive meteorological modeling system—RAMS. *Meteor. Atmos. Phys.*, **49**, 69–91.
- Posselt, D. J., S. C. van den Heever, and G. L. Stephens, 2008: Trimodal cloudiness and tropical stable layers in simulations of radiative convective equilibrium. *Geophys. Res. Lett.*, **35**, L08802, doi:10.1029/2007GL033029.
- , —, —, and M. R. Igel, 2012: Changes in the interaction between tropical convection, radiation, and the large-scale circulation in a warming environment. *J. Climate*, **25**, 557–571.
- Riehl, H., and J. S. Malkus, 1958: On the heat balance in the equatorial trough zone. *Geophysica*, **6**, 503–538.
- Romps, D. M., and Z. Kuang, 2010: Do undiluted convective plumes exist in the upper tropical troposphere? *J. Atmos. Sci.*, **67**, 468–484.
- Saleeby, S. M., and W. R. Cotton, 2004: A large-droplet mode and prognostic number concentration of cloud droplets in the Colorado State University Regional Atmospheric Modeling System (RAMS). Part I: Module descriptions and supercell test simulations. *J. Appl. Meteor.*, **43**, 182–195.
- , and S. C. van den Heever, 2013: Developments in the CSU-RAMS aerosol model: Emissions, nucleation, regeneration, deposition, and radiation. *J. Appl. Meteor. Climatol.*, in press.
- Seigel, R. B., and S. C. van den Heever, 2012: Dust lofting and ingestion by supercell storms. *J. Atmos. Sci.*, **69**, 1453–1473.
- Smagorinsky, J., 1963: General circulation experiments with the primitive equations. I. The basic experiment. *Mon. Wea. Rev.*, **91**, 99–164.
- Stephens, G. L., S. C. van den Heever, and L. Pakula, 2008: Radiative-convective feedbacks in idealized states of radiative-convective equilibrium. *J. Atmos. Sci.*, **65**, 3899–3916.

- Stith, J. L., J. E. Dye, A. Bansemer, A. J. Heymsfield, C. A. Grainger, W. A. Petersen, and R. Cifelli, 2002: Microphysical observations of tropical clouds. *J. Appl. Meteor.*, **41**, 97–117.
- Storer, R. L., and S. C. van den Heever, 2013: Microphysical processes evident in aerosol forcing of tropical deep convective clouds. *J. Atmos. Sci.*, **70**, 430–446.
- Tao, W.-K., and J. Simpson, 1993: The Goddard Cumulus Ensemble model. Part I: Model description. *Terr. Atmos. Oceanic Sci.*, **4**, 19–54.
- , J. R. Scala, B. Ferrier, and J. Simpson, 1995: The effect of melting processes on the development of a tropical and a midlatitude squall line. *J. Atmos. Sci.*, **52**, 1934–1948.
- Tompkins, A. M., and G. C. Craig, 1998: Radiative–convective equilibrium in a three-dimensional cloud-ensemble model. *Quart. J. Roy. Meteor. Soc.*, **124**, 2073–2097.
- van den Heever, S. C., and W. R. Cotton, 2004: The impact of hail size on simulated supercell storms. *J. Atmos. Sci.*, **61**, 1596–1609.
- , G. L. Stephens, and N. B. Wood, 2011: Aerosol indirect effects on tropical convection characteristics under conditions of radiative–convective equilibrium. *J. Atmos. Sci.*, **68**, 699–718.
- Xu, K.-M., and D. A. Randall, 1999: A sensitivity study of radiative–convective equilibrium in the tropics with a convection-resolving model. *J. Atmos. Sci.*, **56**, 3385–3400.
- Yeo, K., and D. M. Romps, 2013: Measurement of convective entrainment using Lagrangian particles. *J. Atmos. Sci.*, **70**, 266–277.
- Zipser, E. J., 1977: Mesoscale and convective–scale downdrafts as distinct components of squall-line structure. *Mon. Wea. Rev.*, **105**, 1568–1589.
- , 2003: Some views on “hot towers” after 50 years of tropical field programs and two years of TRMM data. *Cloud Systems, Hurricanes, and the Tropical Rainfall Measuring Mission (TRMM)*, *Meteor. Monogr.*, No. 51, Amer. Meteor. Soc., 49–58.
- , and M. A. LeMone, 1980: Cumulonimbus vertical velocity events in GATE. Part II: Synthesis and model core structure. *J. Atmos. Sci.*, **37**, 2458–2469.